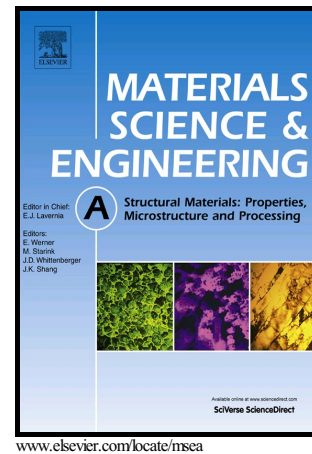


Author's Accepted Manuscript

Corner fatigue cracking behavior inside hybrid laser AA7020 welds by synchrotron X-ray computed microtomography

S.C. Wu, C. Yu, P.S. Yu, J.Y. Buffière, L. Helfen, Y.N. Fu



PII: S0921-5093(15)30600-6
DOI: <http://dx.doi.org/10.1016/j.msea.2015.11.011>
Reference: MSA32991

To appear in: *Materials Science & Engineering A*

Received date: 22 August 2015
Revised date: 5 November 2015
Accepted date: 6 November 2015

Cite this article as: S.C. Wu, C. Yu, P.S. Yu, J.Y. Buffière, L. Helfen and Y.N. Fu, Corner fatigue cracking behavior inside hybrid laser AA7020 welds by synchrotron X-ray computed microtomography, *Materials Science & Engineering A*, <http://dx.doi.org/10.1016/j.msea.2015.11.011>

This is a PDF file of an unedited manuscript that has been accepted for publication. As a service to our customers we are providing this early version of the manuscript. The manuscript will undergo copyediting, typesetting, and review of the resulting galley proof before it is published in its final citable form. Please note that during the production process errors may be discovered which could affect the content, and all legal disclaimers that apply to the journal pertain.

Corner fatigue cracking behavior inside hybrid laser AA7020 welds by synchrotron X-ray computed microtomography

S.C. Wu^{a,*}, C. Yu^a, P.S. Yu^b, J.Y. Buffière^c, L. Helfen^{d,e}, Y.N. Fu^f

^aState Key Lab. of Traction Power, Southwest Jiaotong University, Chengdu 610031, PR China

^bJiangsu Key Lab. of Advanced Manufacturing Equipment & Technology, Jiangnan University, Wuxi 214122, PR China

^cUniversité de Lyon, INSA-Lyon, MATEIS CNRS UMR 5510, 69621 Villeurbanne, France

^dInstitute for Photon Science and Synchrotron Radiation/ANKA, Karlsruhe Institute of Technology, 76131 Karlsruhe, Germany

^eEuropean Synchrotron Radiation Facility (ESRF), BP 220, F-38043 Grenoble Cedex, France

^fShanghai Synchrotron Radiation Facility, Shanghai Institute of Applied Physics, Shanghai 201204, China

Abstract: To elucidate the fatigue corner cracking behaviors related with gas pores of hybrid laser arc welded 7020-T651 alloys, both high resolution in situ synchrotron X-ray computed microtomography and finite element based predictions containing the closure effect or significant plasticity have been undertaken in the domain of fracture mechanics. It is found that fatigue cracks are preferentially initiated from a breaking pore intersecting with the corner free surface and that it steadily propagates inside the weld with a quarter elliptical shape. Moreover, the fatigue corner crack exhibits a very complex morphology. A quantitative agreement between the experiment and prediction of crack shape under executed loading cycles is observed. By using the critical stress intensity factor along the crack line, the modified fracture toughness of a given hybrid laser weld can also be determined numerically for three-dimensional non-penetration curved fatigue cracks.

Keywords: Fatigue crack initiation and propagation; Aluminum alloy; Hybrid laser welding; Synchrotron radiation X-ray 3D imaging; Finite element method

1. Introduction

Currently, fusion welded structures have been extensively applied in the industrial manufacturing of modern sea, ground and airborne transportation vehicles such as high speed naval vessels, railway trains, aircrafts, spacecrafts and many more. However based on the fractography, for fusion welded aluminum alloys components, some metallurgical defects such as gas porosity produced during the solidification seemingly control the

*Corresponding author. Tel.: +86-18349154280, Fax: +86-28-87600868

Email address: wusc@swjtu.edu.cn (S.C. Wu).

mechanical and fatigue performances in terms of the size, position, morphology and distribution [1,2]. Furthermore, experimental studies have shown that most fatigue failures start from various artificial or intrinsic defects in the vicinity of weld such as pits, scratches, burrs, holes, inclusions, micro-pores, metallurgical flaws and cracks as well as weakened grain boundaries [3]. Unfortunately, these fusion welded defects cannot be completely eliminated in essence even though a set of optimized welding parameters and surface treating are adopted properly, especially for the gas porosity. Therefore, special attention should be paid to improve the fatigue resistance of defective welded structures since the fusion welding process simultaneously produce changes in the microstructure, mechanical properties and internal geometry continuity.

Scanning electron microscopy (SEM) together with optical micrography (OM) is usually employed to gain insight into the microstructure/properties (crack initiation and propagation behavior) relationship of welded materials under reversed loading. Such surface-based crack observation shows that the microstructure might play an important role in the initiation and propagation characteristics of small fatigue cracks. Meanwhile, the influence of temperature, crack closure, loading mode and environment (including humidity, pressure, frequency, etc.) on the fatigue crack growth behavior [4-6] has been quantitatively investigated and has been elaborately incorporated into the classical Paris fatigue crack growth law for the ideally homogeneous materials including the most widely-used cast aluminum alloys, Ti-6Al-4V and austempered ductile cast iron. On the other hand, it is usually agreed that for the low cycle fatigue behavior, welding residual stresses are less important than those within the domain of high cycle fatigue especially when the level of imposed strain is high. These studies also show that the time consumed to nucleate a short crack can represent a significant part of the total lifetime (up to 90%).

In other words, there probably exists a serious under-estimation when removing the short crack phenomenon if the fatigue life of engineering metal structures is described only using the classical Paris law within the intermediate stage [7]. More importantly, the fatigue mechanism and planar cracking behavior revealed by using conventional experimental methods with lower spatial resolution (such as post-mortem fractography and free surface observation based on serial sectioning or polishing) can hardly represent the complete performance of the base materials.

To avoid these deficiencies, numerical approaches such as the finite element method (FEM) or extended FEM (XFEM) are usually employed to simulate the crack growth under cyclic loading and unloading [8,9]. Unfortunately, previous studies about the analysis of three-dimensional (3D) fatigue crack propagation are mostly based on models with significantly simplified geometrical configurations, boundary and initial conditions, external loading mode and homogeneously distributed material properties. In addition, to improve the computational precision, finite element based meshing refinement strategies and remeshing technologies have to be developed and employed in the vicinity of crack tip zone instead of the whole geometry region.

Nevertheless, fatigue crack initiation can not be well simulated even using the advanced XFEM, which fails to predict the fatigue life or residual life of real engineering structures. Moreover, it is to date still not easy to efficiently and accurately simulate 3D crack growth (strong discontinuity) with asperity crack front due to bifurcation and deflection [10,11]. It is evident that such result can not represent the actual service status of a cracked body and thus may not elucidate the fatigue cracking mechanism properly. By extracting the crack evolution and morphology from tomography volume datasets, a defect-configuration based finite element fatigue cracking model can be set up to conduct repeated calculation

under the real loading interval and magnitude [12].

Clear understanding and characterization on the physical mechanisms of fatigue short crack behavior may enable one to improve the microstructure and manufacturing and then to enhance the damage tolerance of welded metallic structures. However, the resolution and sample capacity from foregoing conventional experimental techniques provide very limited information of the 3D crack shape especially about the dynamic evolution inside the materials [13,14]. Recently, third generation high resolution synchrotron radiation X-ray computed microtomography (SR- μ CT) has been well developed and successfully introduced to observe the 3D microstructures of bulk materials [15,16], to assess the crack closure effect [17,18] and to evaluate the porosity effect on fatigue resistance [19-21]. As for the porosity/crack relationship, it has been reported that the fatigue cracks usually propagated into the region with denser porosity [22]. As a non-destructive technique, SR- μ CT can produce 3D images of an internal fatigue crack at length scales from a few tens of micrometers to several hundreds of micrometers.

Pioneer studies mostly focused on cast aluminum alloys and titanium alloys (base metal materials) without being welded together. More importantly, few published papers have discussed the influence of 3D gas micro-pores on the fatigue cracking and its evolution inside fusion aluminum alloy welds by combining the advanced in situ high resolution 3D characterization approaches with numerical modeling. Firstly, the present paper reports detailed investigations of corner fatigue crack initiation and growth from the preferential initiation site of gas pores under low cycle fatigued loads, acquired by in situ fatigue SR- μ CT of hybrid laser arc welded aluminum alloys. Then, in order to correlate the crack morphology with resulting crack growth rate, a 3D crack image-based finite element model in the framework of the linear elastic fracture mechanics incorporating the crack

closure effect is established to permit the simulation of the entire failure process. In this model, crack closure is incorporated by introducing the effective thickness of the specimens to better acquire the fatigue cracking parameters. To perform a successive finite element simulation, the new crack front line is corrected and updated according to the experiment after each crack computation has been completed.

2. Materials and experiments

2.0 mm thick plates of a rolled Al-4.2Zn-1.2Mg (AA7020-T651) were butt joined in the rolling direction by a hybrid welding heat source. Such a hybrid welding system consists of an advanced fiber laser (IPG YRL-4000) and a traditional pulsed gas metal arc (GMA, Fronius TPS4000) [23]. The 7020-T651 alloy is a precipitation strengthened material that is widely applied in the China railway high-speed pantograph and other key welded vehicle structures. Yield tensile and ultimate strengths of the original base metal at room temperature were 319 MPa and 357 MPa, respectively.

To obtain a sound hybrid laser welded joint, hybrid welding parameters were selected as: 3.5 kW for the laser power, 0.4 mm for the focus spot diameter, 1.06 μm for the laser wavelength, 150 mm for the focal length of laser lens, 2.7 kW for the arc power, 9 m/min for the laser traveling speed, 1.25 m^3/h for the shielding gas, 80% for the air humidity, -1 mm for the defocusing distance and ER5356 ($\Phi 1.2$ mm) as the filler metal (Al-4.8Mg alloys). This type of filler materials helps to better alleviate the hot crack sensitivity. Besides, the laser was inclined by approximately 10° and the arc torch was inclined to the sample upper surface at 70° . To prevent any relative movement, the plates were fixed onto a worktable using parallel plate clamps.

After about six months' natural aging, dog-bone-shaped specimens were cut from the hybrid welded plates with smoothed weld shape. To simulate the surface grinding used in

real welds, upper and lower reinforcements of the hybrid joint were removed mechanically, and as a result some pores were then cut by the surface and exposed to the environment. All the specimen surfaces were carefully polished using SiC sand paper (2000 grit). Ultimate and yield tensile strengths of reinforcement-removed joints were measured to be 256 MPa and 210 MPa, respectively. Compared with base metal, the hybrid welded joint presents a satisfactory load-carrying capacity in terms of IIW code, more precisely 71.7% and 65.8% in ultimate strength and yield strength of the base materials can be obtained, respectively. The cross-section of the welded samples studied was of the order of $1 \times 1 \text{ mm}^2$ in Fig.1. This small cross section is required in order to be able to use a small voxel size for imaging the fatigue sample at high resolution.

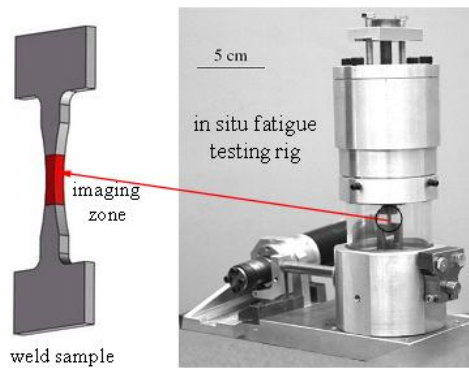


Fig. 1. Schematic shape of hybrid laser weld samples and photograph of the fatigue testing machine to perform the in situ 3D X-ray imaging at ID19 of the ESRF.

The morphology and size of gas pores inside sampled welds were firstly investigated at the 13W1 beam line of the Shanghai Synchrotron Radiation Facility (SSRF) in Shanghai, China [24]. Monochromatic X-ray of 21 keV ($\Delta\lambda/\lambda < 5 \times 10^{-3}$) gave a transmission of at least 30% and a spatial resolution of $0.74 \mu\text{m} \times 2 = 1.48 \mu\text{m}$ was realized in these experiments. The sample was placed at a distance of 25 cm from a 2048×2048 resolution detector and 34 m from the X-ray source. It has been found that gas micro-pores inside hybrid welded high strength Al-Zn-Mg-Cu alloys have a mean sphericity larger than 0.68 and that the equivalent diameter of intrinsic pores ranged from 20 to 80 μm .

The dog bone welded samples for in situ SR- μ CT were investigated at the ID19 beam line of the ESRF with a specially designed fatigue testing machine [25]. The testing rig can conduct high frequency tension-tension loading, which allows for the high cycle fatigue experiments in very limited beamtime. Sinusoidal loading was applied with a load ratio of $R = 0.1$ and a frequency of 20 Hz. The load is transmitted by a polymer tube (PMMA), which permits a 180° rotation without obstruction of the sample and which results in a constant but negligible attenuation of the X-ray beam. In total, 11 samples were prepared and tested at a maximum constant stress of 148 MPa. The chosen photon energy ($\Delta\lambda/\lambda = 10^{-2}$) was 19 keV at ID19 giving a transmission of about 10%. The sample was placed at a distance of 15 cm from a 2048×2048 resolution detector [26], providing an effective isotropic voxel size of $0.7 \mu\text{m}$.

To check the evolution of cracks and micro-pores during fatigued cycling, scans were recorded every 500 cycles with the specimen being held temporarily at peak load, in order to increase crack detectability. A complete scan consisted in a series of 1995 images acquired by rotating over 180° along a vertical axis and the exposure time of each projection was 100 ms. Volume reconstruction was performed slice-wise using a GPU-accelerated filtered back-projection algorithm [27,28].

Binary images of the corner cracks were obtained with ImageJ (region growing thresholding), and visualization was performed with Amira software.

3. Experimental results

3.1 Pore characterization

The morphology and size distribution of gas pores within entire weld were explored at the SSRF and ESRF prior to in situ fatigue. The following Fig.2 presented the typical spatial shape of the corner crack and hybrid weld with metallurgical defects such as micro-pores

in blue. Note here that PM, HAZ and WM stand for the base metal, heat-affected zone and weld metal, respectively. Besides, mature pores and fresh pores denote those grown and newborn micro-pores during the hybrid welding.

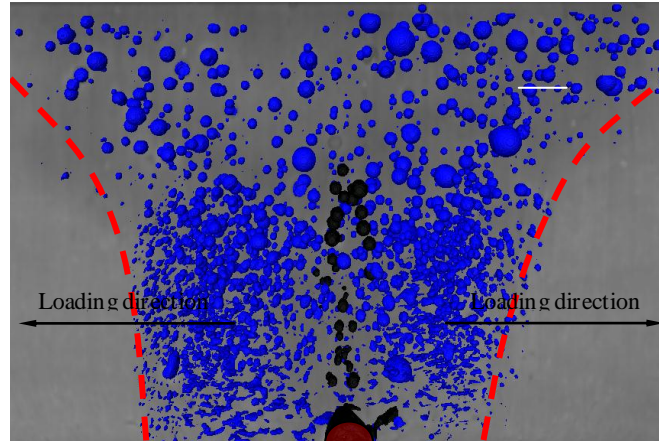


Fig. 2. Rendering of 3D micro-pores in blue as well as the cracking sites in dark inside the weld sample including a crack from a large pore at the corner surface. Note here that black pores in front of initiation pore denoted those cut through by the corner crack.

Two geometric parameters, the effective size (Φ) and the sphericity (Ψ) have been employed to classify the pores. Here Ψ denotes the ratio of the surface area of a sphere (with a volume equal to the pore volume) to that of the gas pore [21]. The smaller the sphericity value, the more irregular the pores shape. To suppress the errors originating from image noise, only those pores larger than $6.33 \mu\text{m}$ (≥ 21 voxels) in diameter were considered in the statistical analysis. The population of gas pores using the above two parameters was shown in Fig.3. Note that the top surface denoted the grinded plane on which upper reinforcement was removed.

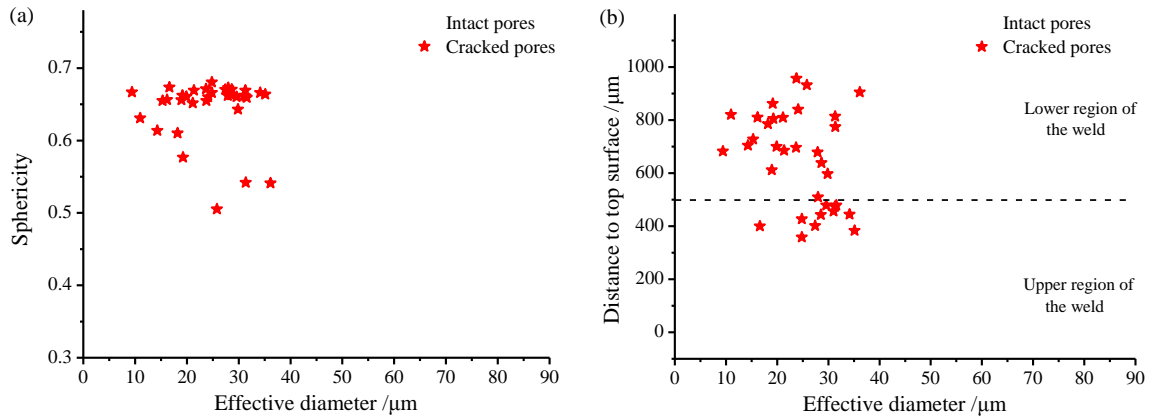


Fig. 3. Relationship between the size and the sphericity and the distance of gravity center of pores to top surface. Red star denoted the pores that were cut across by the crack.

It can be clearly seen from Fig.3a that most of micro-pores larger than 30 μm in effective diameter have a sphericity of approximately 0.60. Although there are still numerous micro-pores with a sphericity smaller than 0.4 inside the weld, this does not mean the existence of pore-like cavity, shrinkage and cracks even when Ψ approaches zero. The fractography observations have shown that the pores with the smaller sphericity might be due to keyhole instability during the welding [29,30]. For cast and rolled engineering materials, such distorted pores or voids were commonly found during various deforming processes associated with broken particles so that elongated shape was usually observed, which are entirely different from the present case.

Besides, only a very small number of micro-pores existed in the upper region of the hybrid weld as shown in Fig.3b, which can be more easily distinguished from Fig.2. In contrast, the lower region has a majority of micro-pores smaller than 25 μm in diameter. During the welding process, very small bubbles are produced when hydrogen rapidly gathers and escape from bottom to top of the weld pool [31]. It may be the vigorous convection and stirring that happened in the melt give a relatively smaller sphericity especially in the early cooling stage. It can be clearly observed from above Fig.2 and Fig.3 that the fatigue crack cut through those inner pores with the effective diameter ranging from 10 to 45 μm and

the mean sphericity of 0.65.

Fig.3 gives the characteristics of gas pores that intersect with the crack plane, as also illustrated in Fig.2 (pores plotted in dark). Such cracked pores had larger sphericity ranging from 0.6 to 0.7 and almost all cracked pores were located in the central region of the hybrid weld. Besides, this figure also shows that the fatigue crack initiates from a large pore at the corner surface and then propagates through the intermediate zone with a typical opening-mode. This interesting point well agrees with the situation shown in Fig.2. It is therefore reasonable to indicate that three factors may affect the crack initiation and propagation: (1) the specimen shape such as the hour glass geometry in Fig.1; (2) the pore distribution in Fig.2; (3) the hardness distribution.

The following Fig.4a illustrates that the central zone of hybrid laser 7020-T651 weld has the lowest hardness due to the serious evaporation of strengthening elements (Fig.4b) and the loss of precipitation effects [32].

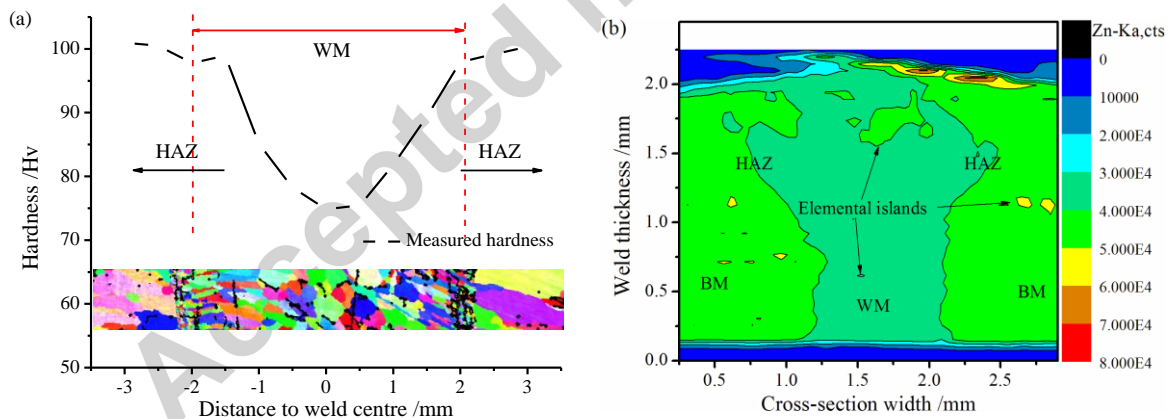


Fig. 4. Hardness profile and element mapping by micro X-ray fluorescence at the cross-section. Note that there were some elemental islands due to the material homogeneity in both WM and BM. The former was formed due to the existence of pores and heterogeneities for the latter.

Besides, only gas pores with diameter in the range of 10-40 μm could be cut through rather than the larger ones in the crack front under cyclic loading, as illustrated in Fig.3.

3.2 Pore-induced cracking

3.2.1 Crack initiation

To reveal the 3D fatigue crack behaviors, a total of 11 weld samples were prepared and examined entirely until fracture happened. By detailed SEM surface observations after grinding, some gas pores were cut partially and were prone to stress concentration under external loading. It can be observed from Fig.5 that fatigue cracks were usually initiated from gas pores near the specimen surface.

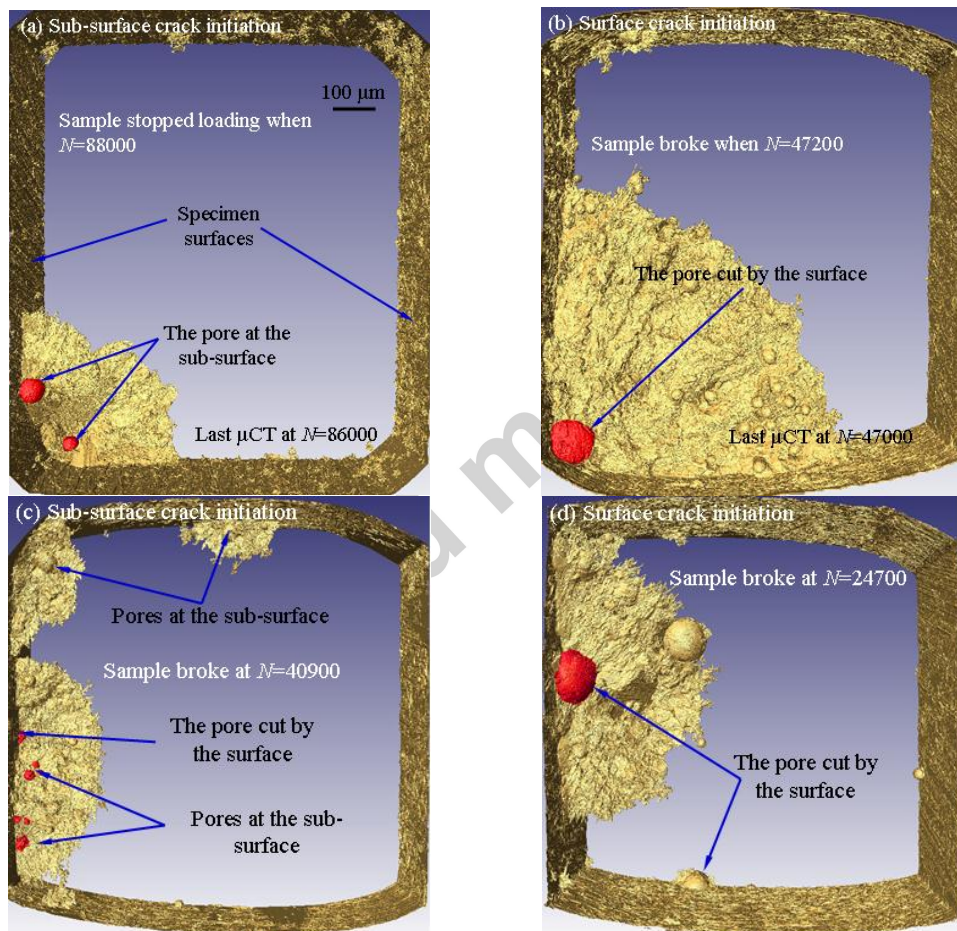


Fig. 5. Fatigue cracking behaviors, where (a) and (b) for a surface corner quarter elliptical crack and (c) and (d) for a typical surface semi-elliptical crack.

Fig.5a and b clearly shows that corner cracks were initiated from pores near the surface and then propagated into a long quarter crack. Note that Fig.5a only provided the intermediate stage of fatigue cracks.

Surface semi-elliptical cracks were also observed in Fig.5c and d, in which Fig.5c demonstrated initiation of a fatigue crack from multi sites (smaller pores) located at both surface and sub-surface while Fig.5d showed another type of regular surface semi-elliptical crack from a single large-size pore. Similar studies have also argued that the most frequently observed site for fatigue crack initiation is surface porosity for a casting Al alloy by using a surface-based observation technique [33]. Current results indicate that inner pores or inclusions hardly contributed to the formation of micro-cracks under low cycle fatigue loading even though they would have a comparative size to or even larger than those pores intersecting with the specimen surface.

The remaining part of this study will focus on the corner fatigue cracking behavior from a broken pore at the free surface, as illustrated in Fig.5b. A series of reconstructed images of a corner crack in the early growth stage was shown in Fig.6.

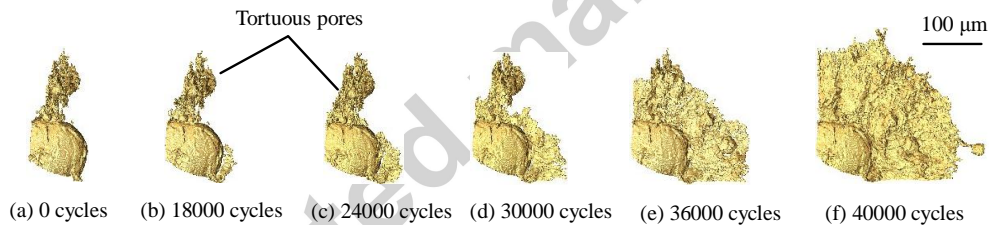


Fig. 6. Propagation evolutions of a corner fatigue crack initiated from a braking pore. The total life of the weld sample was about $N_f = 47200$ cycles.

It was observed that the crack was initiated after about $N_i = 18000$ cycles from a breaking pore that intersects with the corner surface (Fig.6a) primarily due to the grinding process. In other words, the number of cycles to initiate a crack accounts for an assignable part (N_i/N_f is equal to 38% or so, in Fig.6b) of the fatigue life of the sample.

It is worth noting that although inner tortuous pores (also termed as crack-like shrinkages caused during the cooling) appeared to give a serious stress raiser [34], no cracks were initiated in this case. Cracks continued propagating in the weld only if such tortuous pores

were connected by the micro-crack on the right side of a breaking pore. It has been well recognized that this transgranular fatigue crack growth mode was usually followed by an intergranular propagation along a defined crystallographic direction.

3.2.2 Crack propagation

Based on foregoing analyses, it is thus reasonable to define Fig.6a-c as the initiation stage since the crack increment has just exceeded the mean grain size ($\sim 45 \mu\text{m}$ in Fig.6). After the steady stage I cracking, the microstructural short crack grew and then linked crack-like pores (Fig.6a) and surrounding short cracks (Fig.6d), finally exhibiting a representative equilibrium quarter pre-circular or pre-ellipse [35], as illustrated in Fig.6e, f and Fig.7. Compared with relatively regular cracks observed at the free surface, this type of complexly propagating physically short crack has been extensively observed to agree with previous observations for metal structural materials [36].

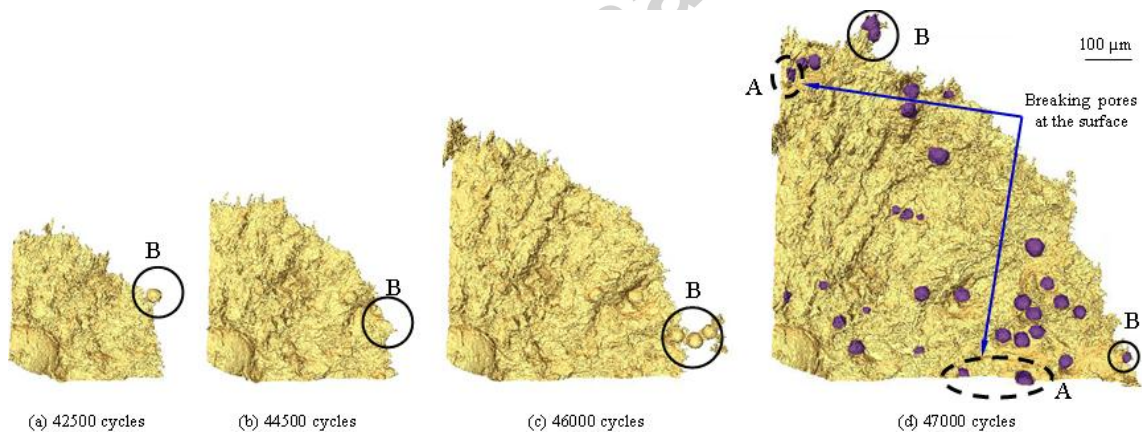


Fig. 7. Long crack propagated stably (Stage II) and suddenly fracture at $N = 47200$.

Fig.6 and Fig.7 show that the crack steadily grow in size and propagated inside the sample. Moreover, the crack development was globally perpendicular to the loading direction, thus giving a typical mode I cracking. It is also very clearly observed from Fig.7c that the crack significantly grows in terms of the size. Such stage II cracking (from Fig.6b with $N = 18000$ cycles to Fig.7c with $N = 46000$ cycles) can be therefore defined to further

characterize the cracking mechanism. The lifetime of intermediate region is about 60% of total cycles of the sample. Then the sample suddenly fractured after 1200 cycles ($N_f = 47200$), representing approximately 2% of the sample lifetime.

Since the 3D tomographic views can provide direct access to geometrical and morphological parameters of accurate details on crack surface in the bulk of the weld, Fig.2 presents the simple analysis of cracking behaviors.

Close observations revealed that some segments of the crack front were slightly retarded or notably accelerated at a given fatigued cycles, as suggested through stochastic microstructures [37]. Fig.5 clearly shows that the crack appears irregular mainly due to grain boundaries and gas porosity near the crack front [36]. For example, due to the existence of micro-pores, an advance segment becomes accelerated relatively to the rest of the crack and the stress intensity factor reduces locally. Fig.8 presents the fatigue cracking behaviors (also termed the long crack stage) related with the micro-pores, in which the red and purple regions represent those pores in the bulk of weld and fully cut through by the crack, respectively. It is worth noting that inner pores denoted by solid circle C in Fig.8 may also be those in front of the crack when the crack approaches them and vice versa.

It can be concluded that the micro-pores as illustrated inside two dashed ellipses has very limited influence on the global crack growth rate even though the local acceleration happens frequently. However, the pores cut by the surface (Dashed ellipse A denoted in Fig.7) and micro-pores exactly in front of crack front (Solid circle B denoted in Fig.7 and Fig.8) can induce a totally higher crack growth rate in contrast with inner micro-pores (Dashed ellipses C and D). Therefore, the following finite element modeling will overlook numerous micro-pores. Furthermore, a regular crack shape is then adopted in terms of real 3D data. Such interesting local acceleration phenomenon of the crack at the free surface

can also be observed in Fig.13b in the absence of micro-pores. This appears that the surface-based measure method of either SEM or OM may give an over-estimate of the fatigue crack growth rate for a real engineering component.

However, some crack segments could retard perhaps due to the barriers of grain boundaries. This interesting propagation makes the crack front slightly deviate from an ideal quarter elliptical shape. Consequently, more attention should be paid on identifying the actual microstructural features. Recent progress has suggested that the time-resolved ultrafast polychromatic X-ray diffraction could be used to follow 3D grain morphology in the welding process [38], which probably provided a way to effectively visualize the microstructural evolution in the bulk of fatigue samples.

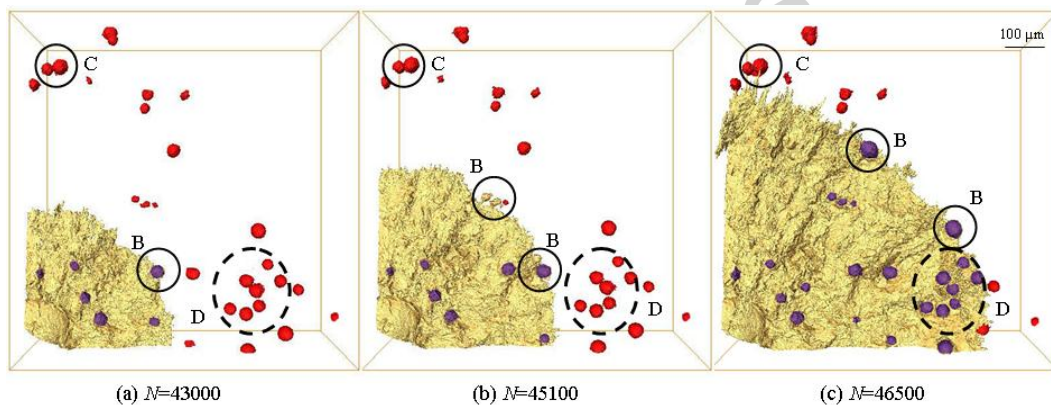


Fig. 8. Long crack behaviors related with the distribution of micro-pores.

For a given number of loading cycles, a range of growth rates can be extracted along the crack front, as illustrated in Fig.5. It is obvious that the cracking rate close to the sample surfaces is approximately the same order to the inner cracks. These variations can be correlated with the presence of grain boundaries and micro-pores. In addition, such observed crack growth anisotropy or discrepancy was probably correlated with the plasticity-induced crack closure. Although a significant acceleration existed when the fatigue crack approached micro-pores, the overall effect of the amplification of crack

advancement along the entire crack path was not pronounced. This conclusion is accurately consistent with reported results [39].

4. Modeling

Based on imaged crack shape and size with micrometer resolution at given loading cycles, a FEM-based model without the gas porosity was built to estimate the fatigue cracking in terms of final fractography data. Moreover, by introducing the effective thickness of a 3D crack tip field, the crack closure effect can be considered into an improved Paris-like law.

Foregoing analyses have shown that the corner fatigue crack is usually initiated from a breaking pore at the corner free surface and then gradually expands to a representative quarter elliptical crack in a short domain of extension. we therefore presumed that it is still feasible to apply the classical elastic fracture mechanics to investigate the cracked specimen despite the fact that crack dimension captured during in situ synchrotron radiation X-ray imaging is shorter than a typical macro crack.

4.1 Crack closure effect

Since observed by Elber in 1970, fatigue crack closure has been one of the critical issues for the quantitative study of fatigue crack propagation [40]. The closure effect can cause a significant deviation of crack growth rate from the initial form of Paris law, which can be modeled in terms of effective stress intensity factor (SIF) range. This important point can be clearly validated from complex crack front as demonstrated from Fig.5 to Fig.8. By considering the crack closure effect, the crack propagation rate model described by the Paris law can be rewritten as

$$\frac{da}{dN} = C_{\text{eff}} (\Delta K_{\text{eff}})^{n_{\text{eff}}} \quad (1)$$

$$\Delta K_{\text{eff}} = \left[\left(1 - \frac{K_{\text{op}}}{K_{\text{max}}} \right) / (1-R) \right] (K_{\text{max}} - K_{\text{min}}) \quad (2)$$

where K_{max} , K_{min} and K_{op} are the SIFs under the maximum, minimum and opening loading, respectively, C_{eff} and n_{eff} are the material parameters that can be determined by fitting simulation results, R is the stress ratio, and the ratio $K_{\text{op}}/K_{\text{max}}$ for a straight-through cracked plate can be taken by [41],

$$\frac{K_{\text{op}}}{K_{\text{max}}} = 1 - \frac{\sqrt{(1-R^2)^2 (1+10.34R^2)}}{\sqrt[3]{\left[1+1.67R^{1.61} + (0.15\pi^2\alpha_g)^{-1} \right]^{4.6}}} \quad (3)$$

where α_g is a combined constraint factor considering 3D stress status of fatigue cracking. By thoroughly analyzing the 3D stress-strain field around the crack tip for a standard Middle Tension specimen, an equivalent thickness B_{eqv} has been well proposed and verified [42]. Such an idea helped to build an equivalent relationship of 3D stress status between the points along a curved crack and a well-defined straight-through crack in a plate of thickness B , thus an empirical formula for calculating the distribution of α_g along a corner crack line was eventually suggested as [43],

$$\alpha_g = \frac{1+0.2088(r_{p0}/B_{\text{eqv}})^{0.5} + 1.5046(r_{p0}/B_{\text{eqv}})}{1-2\nu + 0.2088(r_{p0}/B_{\text{eqv}})^{0.5} + 1.5046(r_{p0}/B_{\text{eqv}})} \quad (4)$$

where ν is Poisson's ratio, $r_{p0} = (\pi/8) \cdot (K_{\text{max}}/\sigma_0)^2$ in the plane stress case. The flow stress σ_0 is taken as the average value between the uniaxial yield and ultimate tensile strength of such hybrid weld. It is interesting to note that the equivalent thickness has been successfully used to predict the fracture loading for a corner cracked structure of aluminum alloy [42,44] as well as the crack opening stress and fatigue life of 7075-T6 aluminum alloy plate specimens containing surface cracks [45].

Conveniently, the B_{eqv} for a point at the quarter elliptic corner crack front line can be evaluated using the following empirical formula,

$$B_{\text{eqv}} = \frac{\pi}{4} c \left[1 - \varphi_u^{4t} \right] \quad (5)$$

$$\varphi_u = \begin{cases} \left(\frac{\pi}{4} \sqrt{t} - \varphi \right) / \frac{\pi}{4} \sqrt{t}, & \text{for } \varphi < \frac{\pi}{4} \sqrt{t} \\ \left(\varphi - \frac{\pi}{4} \sqrt{t} \right) / \left(\pi/2 - \frac{\pi}{4} \sqrt{t} \right), & \text{for } \varphi \geq \frac{\pi}{4} \sqrt{t} \end{cases} \quad (6)$$

where c is the major axis of the ellipse, t is the aspect ratio of ellipse determined as the ratio of the minor to major axis, and φ is the directional angle.

4.2 Crack growth modeling

From the reconstructed data, the geometry of sampled weld with a corner crack-like pore and the adopted coordinates can be established as shown in Fig.9. The geometrical and material parameters of hybrid laser welded specimens were taken as: the initial crack dimension $c = a = 0.2$ mm in terms of initial growth of fatigue crack, the cross section 1×1 mm² for the specimen with the 2 mm height as the representative volume, Young's modulus $E = 64.9$ GPa and Poisson's ratio $\nu = 0.33$.

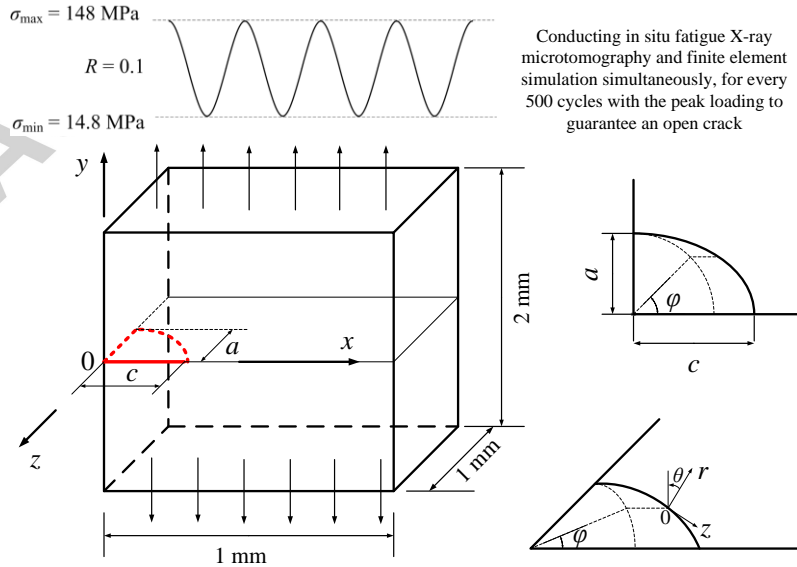


Fig. 9. Schematic geometries of the specimen and a corner crack and fatigue loading mode containing a corner breaking pore for the grinded hybrid weld. Note that θ and r are the axial and radial directions of the local cylindrical coordinates at the crack front line, respectively.

It is worth noting that the studied volume of interest is about $1 \times 1 \times 2 \text{ mm}^3$ (Fig.9), indicating the hybrid weld region containing the typical surface fatigue corner crack. Such small dimension is sufficient enough to representing a local material region with relatively homogeneous properties inside the weld (Fig.4), although hybrid laser 7020-T651 joints exhibit a typical inhomogeneous and anisotropic feature in microstructure. Thus by introducing the parameter of effective thickness B_{eqv} , the crack closure can be incorporated into the crack growth model.

The crack growth simulation can be divided into three steps: initialization, finite element analyses and new crack front line update. The first step is dedicated to define the geometry, initial crack shape, material properties, loadings and boundary conditions and other computation parameters. The second step is to calculate the SIF distribution along crack front line. The last step is responsible for producing a new crack front line which consists of the predictions of effective SIF ranges, crack growth increments from the B_{eqv} -based crack growth model and new crack front line fitted by a cubic spline. The new nonlinear crack front line is then input as the initial crack configuration for the next fatigue cycling. An ANSYS-APDL re-meshing program package was also developed to automatically implement the computation step by step.

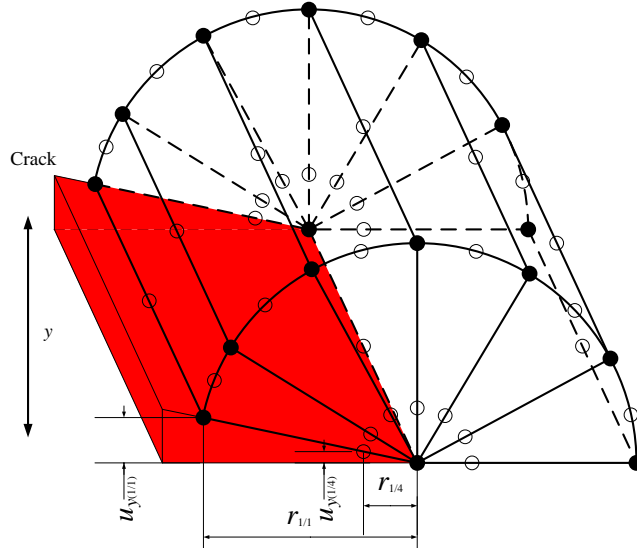


Fig. 10. A schematic diagram for the displacements and spatial arrangements of finite element nodes in singular elements at the crack tip.

The FEM model provides an efficient route to calculate the SIFs based on the 1/4 node singular elements proposed by Barsoum [46]. The SIF can be calculated by fitting the nodal displacements in the vicinity of curved crack. For mode I crack under the plane strain state, the SIF can be calculated by

$$K_I = \frac{E\sqrt{2\pi}}{12(1-\nu^2)} \left(\frac{4u_{y(1/4)}}{\sqrt{r_{1/4}}} - \frac{u_{y(1/1)}}{\sqrt{r_{1/1}}} \right) \quad (7)$$

where $u_{y(1/4)}$ and $u_{y(1/1)}$ are the displacements of the 1/4 node and 1/1 node at the crack surface, $r_{1/4}$ and $r_{1/1}$ are the distances of the 1/4 node and 1/1 node away from the crack tip, respectively, as shown in Fig.10.

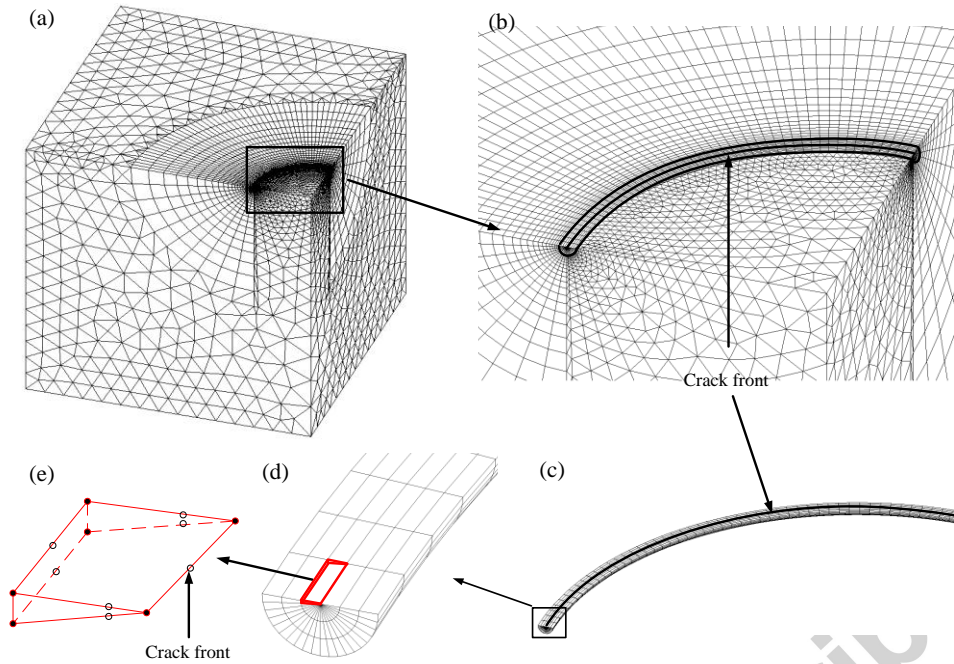


Fig. 11. The finite element model of welded specimen with a corner crack: (a) a typical finite element model of 1/2 plate, (b) the meshes near the crack front, (c) top view of the surrounded meshes of crack front line, (d) detail with enlarged scale of the segment near the free surface and (e) nodes of the first element layer.

Due to the symmetry shown in Fig.9, only one half of the weld model is analyzed. Fifty element layers are arranged along the crack front line. The finite element meshes for a typical corner crack is illustrated in Fig.11a. Note here that only the fatigue crack propagation process can be simulated when the crack broke through the microstructural barrier as defined in Fig.6c.

The accuracy of the FE simulation mainly depends on the refinement strategy of the elements especially surrounding the crack tip singular field. For the current modeling, the element size gradually decreases with the distance approaching the crack border in order to accommodate the sharp variation of the stress and strain near the crack tip. To acquire the SIF along the crack front line in an efficient and accurate scheme, two sets of meshes with different refinement strategies are undertaken and compared. Fig.12 presents the calculation comparison of SIF results.

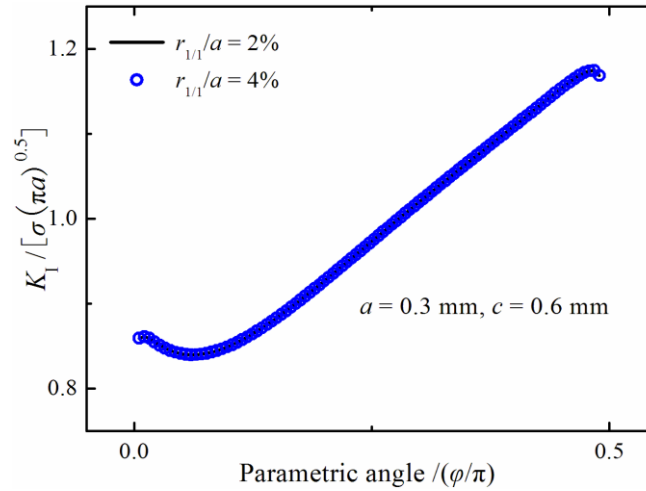


Fig. 12. The SIFs along crack line obtained based on two levels of element size for the first layer surrounding crack tip.

It can be clearly seen that the two meshing strategies (in the first layer surrounding the crack tip) produce exactly coincident results, which shows that the chosen element size in this model is sufficiently refined.

4.3 Updating crack front

From the viewpoint of computational cost in the cycle-to-cycle simulation, creating a new crack front line and re-meshing the model after each loading cycle is impractical and extremely expensive because the total cycles is too large to be completed within acceptable time consumption and computer hardware. Consequently, a summation of every 500 loading cycles is selected as a main loop to reduce the numbers of re-meshing and solving stages. Since the overall crack growth increment of 500 loading cycles is relatively short, the SIF distribution along the crack front line is approximately considered to remain constant in one main loop. Based on the meshing layers of the crack front line, a total of 51 points are used at the node locations along the line. For the j th main loop, the crack growth increment at point i ($1 \leq i \leq 51$) can be obtained by

$$\Delta a_{i,j} = 500C_{\text{eff}} \left(\Delta K_{\text{eff},i,j} \right)^{n_{\text{eff}}} \quad (8)$$

where $\Delta K_{\text{eff},i,j}$ is the effective SIF at point i . Then point i is moved forward a distance of $\Delta a_{i,j}$ along the normal direction of the crack front line. This operation is repeated for all the 51 points in order to create the new point locations. After that, a new line is determined by a cubic spline fitting. Thus, the next loop can be carried out sequentially by inputting the spline as a smoothed crack front line.

5. Estimation of C and n

Finite element simulations for fatigue crack growth provide a practical approach to estimate the crack growth rate based on the crack sizes and growth lives. According to the crack profile observed in the test, the idealized elliptical corner crack is further simplified as a quarter circular with an initial radius of 0.2 mm.

For the first main loop, C_{eff} and n_{eff} are empirically estimated and then the simulations are conducted automatically based on the ANSYS-APDL routine. When the crack propagates to the maximum size measured in the experiment, the current main loop is quit and the recorded historical crack profiles with cycle numbers are compared with available experimental results. After that, the values of C_{eff} and n_{eff} are adjusted according to the error between the simulations and experiments, and the updated C_{eff} and n_{eff} are then input to the program for the next main loop to achieve better consistency between the simulations and experiment. This process is repeated automatically until C_{eff} and n_{eff} converge to stable values. For crack growth dimensions of mm/cycle, the best fitting of crack profile and required loading cycles suggests as $C_{\text{eff}} = 4.5 \times 10^{-7}$, $n_{\text{eff}} = 5.4$.

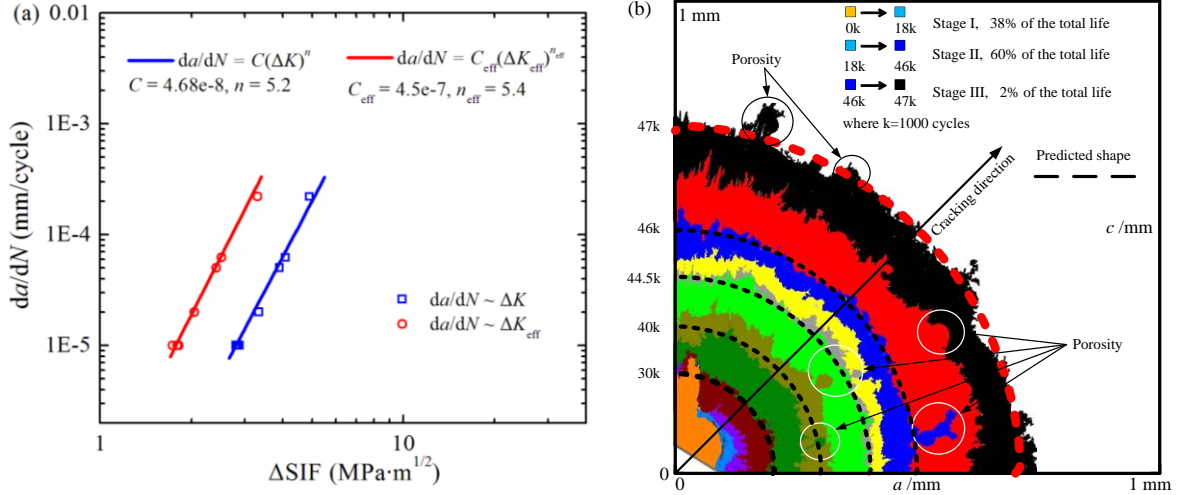


Fig. 13. Comparison of prediction with experiment results: (a) Calculated crack growth rate curve with and without considering closure effect; (b) Superimposed crack growth front evolutions based on finite element simulation and in situ fatigue imaging experiment.

For the traditional ΔK -based Paris law without the closure effect,

$$\frac{da}{dN} = C(\Delta K)^n \quad (9)$$

The predicted parameters are determined by the above mentioned steps of simulations: $C = 4.68 \times 10^{-8}$ and $n = 5.2$, which are slightly smaller than those from improved fatigue cracking model considering the crack closure effect.

Even both the ΔK_{eff} - and ΔK - based parameters are obtained based on the test data, the C_{eff} and n_{eff} are considered as the real material constants while the C and n are usually dependent on stress ratio and specimen geometry. Therefore, to predict the crack growth life for given stress ratio or specimen geometry different from the current test, the C_{eff} and n_{eff} could be used directly while the C and n would not work well due to their strong dependence on the stress ratio and specimen geometry.

The baseline of the crack growth rate and the comparison of total crack growth cycles and crack configurations between the simulations and experiments can be found in Fig.13a and b, respectively. It can be clearly found that the $da/dN \sim \Delta K$ curve is significantly lower than

that of the $da/dN \sim \Delta K_{\text{eff}}$ curve in the presence of crack closure. This interesting evolution apparently argues that the ΔK_{eff} is more valid than traditional ΔK to drive the fatigue crack growth. It is again verified that the fatigue crack closure can partly determine the real local cracking behaviors. Fig.13b shows a good agreement between numerical predictions (dashed curve) and experimental results in both crack growth rate and, crack shape, which provides very meaningful information to the fatigue resistance design and reliable prediction of welded aluminum alloys.

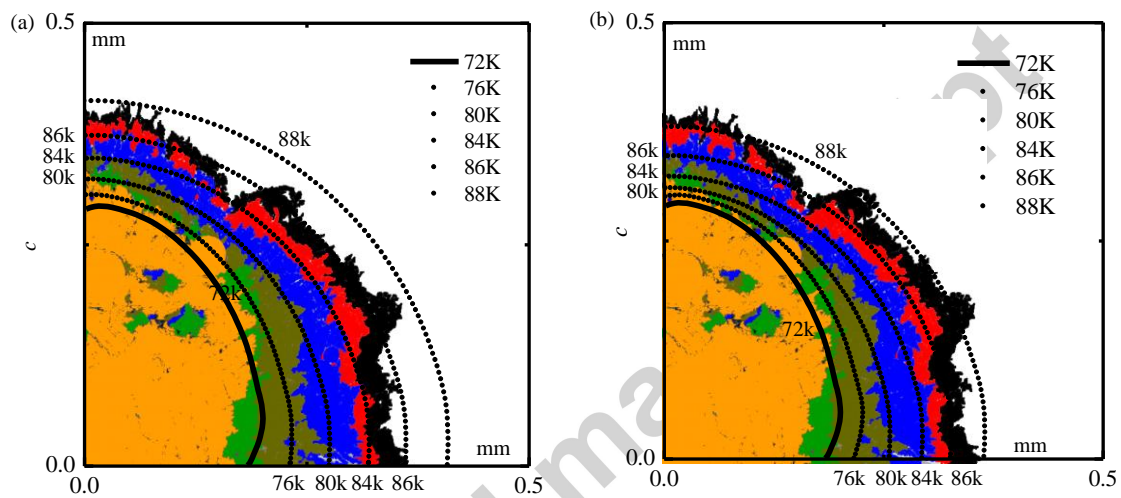


Fig. 14. Comparisons of predicted crack shape from two models to real tomography data, without (a) and with (b) considering the crack closure effect.

To further present the validation of ΔK_{eff} -based fatigue crack law, Fig.14 compared the projected shapes of corner 3D fatigue crack as shown in Fig.5a to the calculated shape in the dashed line. It can be clearly seen that the ΔK_{eff} -based Paris fatigue crack law can provide more precise and valid predictions of fatigue cracking life in theory compared with classical Paris law. This point argues that it is remarkably necessary to consider the crack closure. The basic difference from artificial penetration pre-cracked specimen subjected to quasi-static loads provides a very meaningful reference to welded aluminum alloy structures containing surface defects.

6. Conclusions

This study shows detailed results of in situ fatigue synchrotron radiation X-ray computed microtomography of hybrid laser welded 7020-T651 aluminum alloy containing numerous gas micro-pores. Based on high resolution cracking tomography results, finite element simulation combined with real 3D imaging data of crack morphology and corresponding cycles was employed to simulate the corner cracking process including the crack growth rate and crack shape. The crack closure effect is also considered to improve the classical crack growth rate model by introducing the constraint effect. From the present study, some conclusions can be drawn as:

- (1) The fatigue crack inside the hybrid weld is usually initiated from a large surface after surface polishing. The crack steadily evolves into a quarter elliptical shape, eventually resulting in the mode I cracking.
- (2) Only those micro-pores located in the middle of the weld with a mean sphericity of about 0.6 and an effective diameter of around 30 μm were cut through by the crack front from current results. Moreover, it appears that the size and morphology distribution have no pronounced effect on the overall crack development.
- (3) The crack initiation life and propagation life are about 38% and 60% of total loading cycles of sampled weld, respectively, which shows that the short fatigue cracking behaviors are noticeable.
- (4) The predicted crack size and overall shape coincide well with experimental results. Nevertheless, there exists a slight deviation of computed fatigue cracking law parameters of $C_{\text{eff}} = 4.5 \times 10^{-7}$ and $n_{\text{eff}} = 5.4$ compared with measured values. Such difference is reasonable due to intrinsic limitation and imperfection of conventional finite element modeling.

Acknowledgements

The authors give sincere thanks to the National Natural Science Foundation of China (11572267, 11302067), the Self-developed Research Project of the State Key Lab. of Traction Power (2015TPL_T07) and the Fundamental Research Funds for the Central Universities (B12020031).

References

- [1] J.F. Rudy, E.J. Rupert, *Weld. J.* 49 (1970): 322-336.
- [2] R.C. Andrew, J. Waring, *Weld. J.* 53 (1974): 85-87.
- [3] S. Suresh, *Fatigue of Materials*, Cambridge university press, Cambridge, 1998.
- [4] J.Z. Yi, Y.X. Gao, P.D. Lee, T.C. Lindley, *Metall. Mater. Trans. B* 37 (2006): 301-311.
- [5] C. Sarrazin-Baudoux, Y. Chabanne, J. Petit, *Scripta Mater.* 40 (1999): 451-457.
- [6] J. Crapps, S. Daniewicz, *Int. J. Fatigue* 45 (2012): 15-30.
- [7] B.L. Josefson, J.W. Ringsberg, *Int. J. Fatigue* 31 (2009): 1413-1421.
- [8] J. Barés, L. Gélébart, J. Rupil, L. Vincent, *Int. J. Fatigue* 44 (2012): 279-291.
- [9] S.R. Daniewicz, S. Ismonov, *Int. J. Fatigue* 32 (2010): 428-433.
- [10] J. Rannou, N. Limodin, J. Réthoré, A. Gravouil, W. Ludwig, M.C. Baietto-Dubourg, J.Y. Buffière, A. Combescure, F. Hild, S. Roux, *Comput. Meth. Appl. Mech. Eng.* 199 (2010): 1307-1325.
- [11] M.R. Seabra, P. Šuštarčič, J.M.C. De Sa, T. Rodič, *Comput. Mech.* 52 (2013): 161-179.
- [12] L. Qian, H. Toda, S. Nishido, T. Kobayashi, *Acta Mater.* 54 (2006): 4881-4893.
- [13] S.R. Stock, *Int. Mater. Rev.* 44 (1999): 141-164.
- [14] P.J. Withers, M. Preuss, *Annu. Rev. Mater. Res.* 42 (2012): 81-103.
- [15] H. Toda, T. Kobayashi, M. Niinomi, T. Ohgaki, M. Kobayashi, N. Kuroda, T. Akahori, K. Uesugi, K. Makii, Y. Aruga, *Metall. Mater. Trans. A* 37 (2006): 1211-1219.
- [16] M. Herbig, A. King, P. Reischig, H. Proudhon, E.M. Lauridsen, J. Marrow, J.Y. Buffière, W. Ludwig, *Acta Mater.* 59 (2011): 590-601.
- [17] H. Toda, I. Sinclair, J.Y. Buffière, E. Maire, T. Connolley, M. Joyce, K.H. Khor, P. Gregson, *Philos. Mag.* 83 (2003): 2429-2448.
- [18] K.H. Khor, J.Y. Buffière, W. Ludwig, I. Sinclair, *Scripta Mater.* 55 (2006): 47-50.
- [19] J.Y. Buffière, S. Savelli, P.H. Jouneau, E. Maire, R. Fougères, *Mater. Sci. Eng. A* 316 (2001): 115-126.
- [20] N. Vanderesse, E. Maire, A. Chabod, J.Y. Buffière, *Int. J. Fatigue* 33 (2011): 1514-1525.
- [21] E. Padilla, V. Jakkali, L. Jiang, N. Chawla, *Acta Mater.* 60 (2012): 4017-4026.
- [22] H. Zhang, H. Toda, H. Hara, M. Kobayashi, T. Kobayashi, D. Sugiyama, N. Kuroda, K. Uesugi, *Metall. Mater. Trans. A* 38 (2007): 1774-1785.
- [23] S.C. Wu, X. Yu, R.Z. Zuo, W.H. Zhang, H.L. Xie, J.Z. Jiang, *Weld. J.* 92 (2013): 64-71.
- [24] S.C. Wu, C. Yu, W.H. Zhang, Y.N. Fu, L. Helfen, *Sci. Technol. Weld. Join.* 19 (2014): 732-744.
- [25] N. Limodin, J. Réthoré, J.Y. Buffière, F. Hild, S. Roux, W. Ludwig, J. Rannou, A. Gravouil, *Acta Mater.* 58 (2010): 2957-2967.
- [26] P.A. Douissard, A. Cecilia, X. Rochet, X. Chapel, T. Martin, K.T. Van De, L. Helfen, T. Baumbach, L. Luquot, X. Xiao, J. Meinhardt, A. Rack, *J. Instrum.* 7 (2012): P09016.
- [27] S. Chilingaryan, A. Mirone, A. Hammersley, C. Ferrero, L. Helfen, A. Kopmann, T.D.S. Rolo, P.A. Vagovic, *IEEE Trans. Nuc. Sci.* 58 (2011): 1447-1455.
- [28] A. Mirone, E. Brun, E. Gouillart, P. Tafforeau, J. Kieffer, *Nuc. Instrum. Methods Phys. Res. Sec B: Beam Intera. Mater. Atoms*, 324 (2014): 41-48.
- [29] B. Hu, I.M. Richardson, *J. Laser Appl.* 17 (2005): 70-80.
- [30] S. Beretta, B. Previtali, *Sci. Technol. Weld. Join.* 14 (2009): 106-116.
- [31] J.L. Huang, N. Warnken, J.C. Gebelin, M. Strangwood, R.C. Reed, *Acta Mater.* 60 (2012): 3215-3225.

- [32] A. Deschamps, S. Ringeval, G. Texier, D.L. Delfaut, *Mater. Sci. Eng. A* 517 (2009): 361-368.
- [33] H.R. Ammar, A.M. Samuel, F.H. Samuel, *Mater. Sci. Eng. A* 473 (2008): 58-64.
- [34] F. Bouafia, S. Boualem, M.M.E. Amin, B. Benali, *Comput. Mater. Sci.* 50 (2011): 1450-1459.
- [35] J.Y. Buffière, E. Ferrie, H. Proudhon, W. Ludwig, *Mater. Sci. Tech.* 22 (2006): 1019-1024.
- [36] W. Ludwig, J.Y. Buffière, S. Savelli, P. Cloetens, *Acta Mater.* 51 (2003): 585-598.
- [37] B.N. Cox, W.L. Morris, *Eng. Fract. Mech.* 31 (1988): 591-610.
- [38] W.U. Mirihanage, M. Di Michiel, A. Reiten, L. Arnberg, H.B. Dong, R.H. Mathiesen, *Acta Mater.* 68 (2014): 159-168.
- [39] E. Ferrié, J.Y. Buffière, W. Ludwig, A. Gravouil, L. Edwards, *Acta Mater.* 54 (2006): 1111-1122.
- [40] N. Limodin, J. Réthoré, J.Y. Buffière, A. Gravouil, F. Hild, S. Roux, *Acta Mater.* 57 (2009): 4090-4101.
- [41] T.C. Chang, W.L. Guo, *Eng. Fract. Mech.* 64 (1999): 59-65.
- [42] P.S. Yu, C.M. She, W.L. Guo, *Int. J. Solids Struct.* 47 (2010): 2123-2130.
- [43] G.L. Guo, *Eng. Fract. Mech.* 62 (1999): 383-407.
- [44] S. Pitt, R. Jones, *Eng. Fail. Anal.* 8 (2001): 371-397.
- [45] I.S. Putra, J. Schijve, *Fat. Fract. Eng. Mater. Struct.* 15 (1992): 323-338.
- [46] R.S. Barsoum, *Int. J. Numer. Methods Eng.* 10 (1976): 25-37.

Accepted manuscript